Metal–Organic Frameworks Hot Paper

How to cite: *Angew. Chem. Int. Ed.* **2022,** *61,* e202117565
International Edition: doi.org/10.1002/anie.202117565
German Edition: doi.org/10.1002/ange.202117565

Tuning the High-Pressure Phase Behaviour of Highly Compressible Zeolitic Imidazolate Frameworks: From Discontinuous to Continuous Pore Closure by Linker Substitution

*Jianbo Song, Roman Pallach, Louis Frentzel-Beyme, Pascal Kolodzeiski, Gregor Kieslich, Pia Vervoorts, Claire L. Hobday, and Sebastian Henke**

Abstract: The high-pressure behaviour of flexible zeolitic imidazolate frameworks (ZIFs) of the ZIF-62 family with the chemical composition $M(im)_{2-x}(bim)_x$ is presented ($M^{2+}=Zn^{2+}$, Co^{2+}; im^- = imidazolate; bim^- = benzimidazolate, $0.02 \le x \le 0.37$). High-pressure powder X-ray diffraction shows that the materials contract reversibly from an open pore (***op***) to a closed pore (***cp***) phase under a hydrostatic pressure of up to 4000 bar. Sequentially increasing the bim^- fraction (x) reinforces the framework, leading to an increased threshold pressure for the ***op***-to-***cp*** phase transition, while the total volume contraction across the transition decreases. Most importantly, the typical discontinuous ***op***-to-***cp*** transition (first order) changes to an unusual continuous transition (second order) for $x \ge 0.35$. This allows finetuning of the void volume and the pore size of the material continuously by adjusting the pressure, thus opening new possibilities for MOFs in pressure-switchable devices, membranes, and actuators.

Introduction

Responsive materials that drastically change their physical properties depending on their environment are of great significance for the development of novel energy-efficient technologies.[1–3] Among these, flexible metal–organic frameworks (MOFs)[4,5] are a highly tuneable family of responsive porous materials, which may find applications in gas[6,7] and energy[8] storage, molecular separation[9] and sensing.[10,11] Typical flexible MOFs undergo first-order phase transitions between two distinct states of largely different porosity and density in response to various stimuli,[12] most prominently the ad-/desorption of guest molecules or changes in temperature.[4,12–16] A large body of previous work demonstrated that the responsive properties of flexible MOFs can be adjusted by exchanging or tuning the corresponding inorganic or organic building units of the materials; e.g., by exchanging metal ions or by functionalization of the organic linker,[16] thus offering the possibility of adjusting the material's response for a particular application.[4,5,13,14,17,18]

Besides their response to guest adsorption and temperature, the reaction of flexible MOFs to mechanical pressure has received more and more attention recently, not only due to its relevance for shaping and pelletizing MOFs for applications in catalysis and sorption, but also for the exploration of new applications, such as shock absorbers or dampers.[19–24] Several derivatives of the MIL-47/MIL-53 family (MIL = Matériaux de l'Institut Lavoisier, M(X)(bdc); $M=V^{4+}$, Cr^{3+}, Al^{3+}; $X=O^{2-}$, OH^-, F^-; bdc^{2-} = 1,4-benzenedicarboxylate)[25] have been demonstrated to undergo first-order phase transitions from a large pore (***lp***) to a narrow pore (***np***) phase under application of mechanical pressure.[20,21,23,26] Due to the "winerack-like" structure of these materials, the ***lp***-to-***np*** transition is highly anisotropic, involving a strong framework compression along one direction, which is geometrically coupled to an expansion in the perpendicular direction. A strongly related structural behaviour has been demonstrated for pillared-layered MOFs of the type $M_2(fu\text{-}bdc)_2(dabco)$ ($M^{2+}=Zn^{2+}$, Cu^{2+}; $fu\text{-}bdc^{2-}$ = dialkoxy-functionalized bdc^{2-}, dabco = 1,4-diazabicyclo[2.2.2]octane), which similarly possesses a winerack-like structure.[13,27–30] For MIL-47/MIL-53 materials as well as the pillared-layered MOFs, it was shown that the nature of the metal ion as well as the functionalization of the organic linker influence the transition pressure of the ***lp***-to-***np*** transition.[21,23,26,29,31,32] However, the precise influence of such modifications on the phase behaviour of flexible MOFs is hard to predict, therefore a method that targets the tuning of the supramolecular mechanics of flexible MOFs must be developed.

[*] J. Song, R. Pallach, L. Frentzel-Beyme, P. Kolodzeiski, Prof. S. Henke
Anorganische Materialchemie, Fakultät für Chemie & Chemische Biologie, Technische Universität Dortmund
Otto-Hahn-Straße 6, 44227 Dortmund (Germany)
E-mail: sebastian.henke@tu-dortmund.de

Dr. G. Kieslich, Dr. P. Vervoorts
Department of Chemistry, Technical University of Munich
Lichtenbergstrasse 4, 85748 Garching (Germany)

Dr. C. L. Hobday
Centre for Science at Extreme Conditions and EaStCHEM School of Chemistry, The University of Edinburgh, King's Buildings
West Mains Road, Edinburgh EH9 3FJ (U.K.)

In this work, we demonstrate that the high-pressure mechanical behaviour of a flexible MOF system can be very precisely adjusted by applying the concept of mixed-linker solid solutions. As a flexible MOF platform, we use the established zeolitic imidazolate framework ZIF-4.[34–38] ZIF-4 is composed of tetrahedrally coordinated divalent metal cations M^{2+} (Zn^{2+} or Co^{2+}) and imidazolate (im^-) linkers (Figure 1a), and it exhibits the chemical composition $M(im)_2$ and crystallizes in a zeolite-like network with the **cag** topology in the space group *Pbca*. Previous work revealed that the guest-free ***op*** phase of ZIF-4 transforms to a drastically contracted ***cp*** phase either when vacuum-cooled to temperatures below 140 K[33] or when hydrostatically compressed at pressures between 280 and 5000 bar, the latter depends on the pressure transmitting medium (PTM), the compression rate and the selected metal ion (Zn^{2+} or Co^{2+}).[19,39,40] The framework connectivity is fully preserved while the material contracts almost isotropically by about 23%. Strong contraction is achieved by substantial rotation of the im^- linkers (up to 69.3°) about the M–N bonds, resulting in a 3D inward folding of the framework.[33] The ***op*** phase exhibits a guest-accessible void fraction of 25.9% of the crystal volume, which is eliminated in the ***cp*** phase (Figure 1b; void fraction calculated based on the published crystal structures[33] with geometrically added H atoms using a probe radius of 1.5 Å).

It is established that parts of the im^- linkers in ZIF-4 can be exchanged for bulkier benzimidazolate (bim^-) linkers while network structure and topology remain unchanged. The corresponding materials of the general chemical formula $M(im)_{2-x}(bim)_x$ are known under the name ZIF-62 and have first been reported for $M^{2+} = Zn^{2+}$ and $x = 0.25$.[41] The cobalt derivative with $x = 0.30$ was described later.[42] L. Frentzel-Beyme et al. recently demonstrated that ZIF-62 and ZIF-4 form a continuous solid solution with x ranging from 0 (for ZIF-4) to 0.35.[43] In this context it was shown that x controls the melting temperature of the mixed-linker ZIFs, which is beneficial for the preparation of ZIF glasses[44,45] at lower temperature.

Herein, we investigate the structural behaviour of a series of eight different solid solutions of the ZIF-62 family with high-pressure (HP) powder X-ray diffraction (PXRD) in the pressure range from ambient up to 4000 bar. Supporting insights into the corresponding low-temperature behaviour of the materials was obtained with variable temperature (VT) PXRD in the range from 300 K down to 100 K. We demonstrate that the HP phase behaviour of the materials can be systematically tuned by precisely adjusting

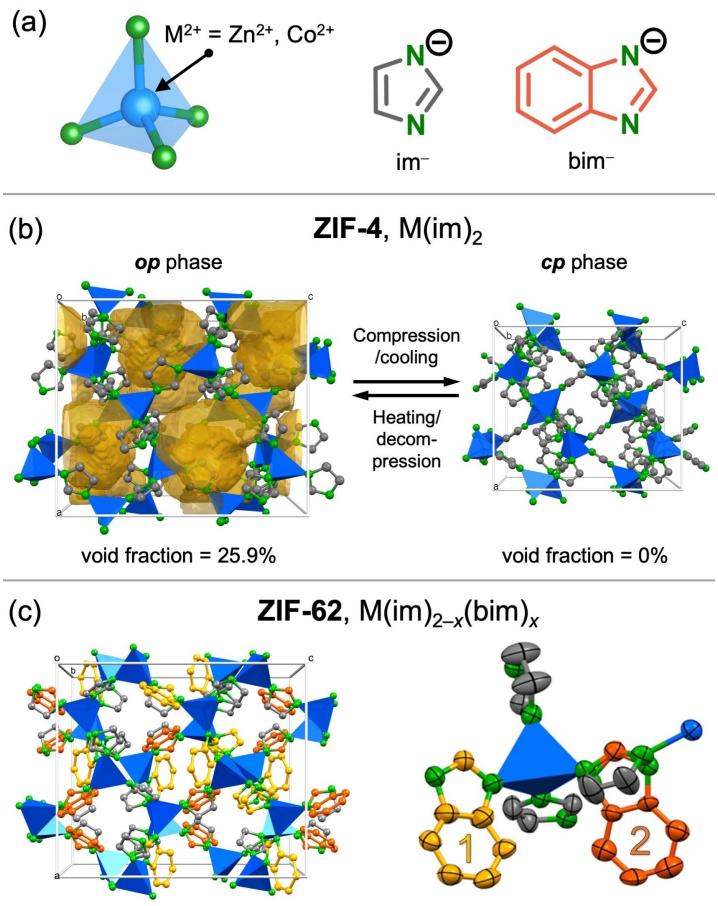

Figure 1. a) The building blocks of ZIF-4 and ZIF-62. B) Representation of the ***op***-to-***cp*** phase transition of ZIF-4 with the available void fraction in the crystal structures[33] highlighted in yellow. C) A single-crystal structure of guest-free ZIF-62 (***op*** phase) from this work showing the unit cell (left) and the asymmetric unit (right), with the partially occupied bim^- linkers at the crystallographically independent positions **1** and **2** highlighted.

the fraction (x) of bim$^-$ in the material, leading to (i) a reinforcement of the frameworks and a shift of the ***op***-to-***cp*** transition pressure to higher pressures, (ii) a concomitant reduction of the volume change (ΔV) across the transition and (iii) the evolution from a discontinuous (first-order) to a continuous (second-order) phase transition with increasing x. Structure refinements on the basis of the HP-PXRD data (Rietveld method)[46,47] establish that the continuous change from the ***op*** to the ***cp*** phase allows adjustment of the pore volume and size of the material precisely by selecting the corresponding pressure. Our work provides a guideline for the targeted finetuning of the supramolecular mechanics of flexible MOFs, setting the stage for their application in pressure-switchable membranes, nanodampers or nanoscopic actuators.

Results and Discussion

Synthesis

Eight different ZIF-62(M)-bim$_x$ solid solutions of the general composition M(im)$_{2-x}$(bim)$_x$ (with $M^{2+} = Zn^{2+}$ or Co^{2+}) and the reference compound ZIF-4(Zn) were prepared according to published procedures (six ZIF-62(Zn)-bim$_x$ samples with $x = 0.02$, 0.05, 0.17, 0.25, 0.30 and 0.35; two ZIF-62(Co)-bim$_x$ materials with $x = 0.27$ and 0.37; see the Supporting Information for details).[41,43] After washing and a solvent-exchange processes, the ZIF single crystals were evacuated under high dynamic vacuum at 120 °C to derive the solvent-free porous crystals. The complete removal of all solvent guests was verified by solid-state FTIR spectroscopy (Supporting Information, Figure S1) as well as liquid-phase ^{1}H NMR spectroscopy of digested ZIF samples (Supporting Information, Section S3). The fraction of bim$^-$ per formula unit (x) was also determined by ^{1}H NMR spectroscopy.

Single-Crystal X-ray Diffraction

Guest-free single crystals of all ZIF-62(M)-bim$_x$ solid solutions were studied with single-crystal X-ray diffraction. All compounds have the **cag** topology and crystallize in the orthorhombic space group *Pbca*, featuring two independent M^{2+} cations and four independent imidazolate-type linkers in the asymmetric unit. In all compounds the bim$^-$ linkers partially occupy two out of the four crystallographically independent linker positions (highlighted as positions **1** and **2** in Figure 1c). For $x = 0.02$, bim$^-$ could only be located at position **1**, while bim$^-$ partially occupies positions **1** and **2** for $x \geq 0.05$ (Supporting Information, Table S2). It is noteworthy that the bim$^-$ linker at position **2** features a significantly different orientation than the smaller im$^-$ linker at the same position, so that unfavourable steric interactions are avoided.

Low-Temperature Powder X-ray Diffraction

The low-temperature behaviour of selected representatives of the ZIF-62(M)-bim$_x$ materials was compared to the behaviour of the highly flexible parent compound ZIF-4(Zn). High-resolution VT-PXRD patterns of carefully ground samples were recorded at beamline P02.1 of PETRA III at DESY (Deutsches Elektronen Synchrotron, Hamburg, Germany) upon cooling the materials from 300 K down to 100 K with data collected every 10 K. In accordance with a previous report,[33] the ***op***-to-***cp*** transition of ZIF-4(Zn) starts at 190 K and is completed at 110 K. Except for ZIF-62(Zn)-bim$_{0.02}$, all of the studied solid solutions ZIF-62(Zn)-bim$_x$ remain in the ***op*** phase when cooled to 100 K. ZIF-62(Zn)-bim$_{0.02}$ shows weak reflections associated with the ***cp*** phase appearing in the VT-PXRD patterns at temperatures below 150 K. However, the ***cp*** phase remains a minority in the diffraction pattern even at 100 K. These results signify that already very small amounts of bim$^-$ have a decisive influence on the potential energy landscape of these materials and thus hamper the transformation to the enthalpically favoured ***cp*** phase. Note that for $x = 0.02$ only 1% of all linkers in the material are bim$^-$ (equal to only 0.32 bim$^-$ linkers per unit cell), while the others are the smaller im$^-$ linkers.

Based on profile fits (Le Bail method),[48] the coefficients of thermal expansion (CTEs) for the ***op*** phases of the ZIF-62(M)-bim$_x$ materials were derived from the temperature-dependent PXRD data. The volumetric CTE at 110 K decreased with increasing x from ca. 600×10^{-6} K^{-1} for ZIF-62(Zn)-bim$_{0.02}$ to only about 100×10^{-6} K^{-1} for ZIF-62(Zn)-bim$_{0.35}$ (the linear CTEs can be found in Section S7 of the Supporting Information). This visualizes the consecutive reinforcement and decreased flexibility of the ZIF-62(M)-bim$_x$ derivatives with increasing x.

High-Pressure Powder X-ray Diffraction

The high-pressure behaviour of the ZIF-62(M)-bim$_x$ derivatives was investigated in the pressure range from ambient up to 4000 bar using a hydraulic pressure cell at beamline I15 of the Diamond Light Source (Oxon., UK).[27,39,49,50] This setup allows collection of high-quality PXRD patterns of soft and flexible MOFs with a high-pressure resolution (pressure step size was 100 bar from ambient to 2000 bar and 250 bar from 2000 to 4000 bar). The guest-free ZIF powders were filled in plastic capillaries together with silicone oil (AP 100) as a non-penetrating PTM and subsequently sealed with adhesive epoxy paste Araldite-2014-1. The HP-PXRD patterns of the ZIF-62(Zn)-bim$_x$ materials are displayed in Figure 2 in the form of contour plots. The corresponding data of the related ZIF-62(Co)-bim$_x$ derivatives are shown in Figure S31. In contrast to the absence of a phase transition in almost all the VT-PXRD experiments, all ZIF samples undergo a transition from the ***op*** to the ***cp*** phase (both feature the same orthorhombic space group *Pbca*) through the stimulus of mechanical pressure.

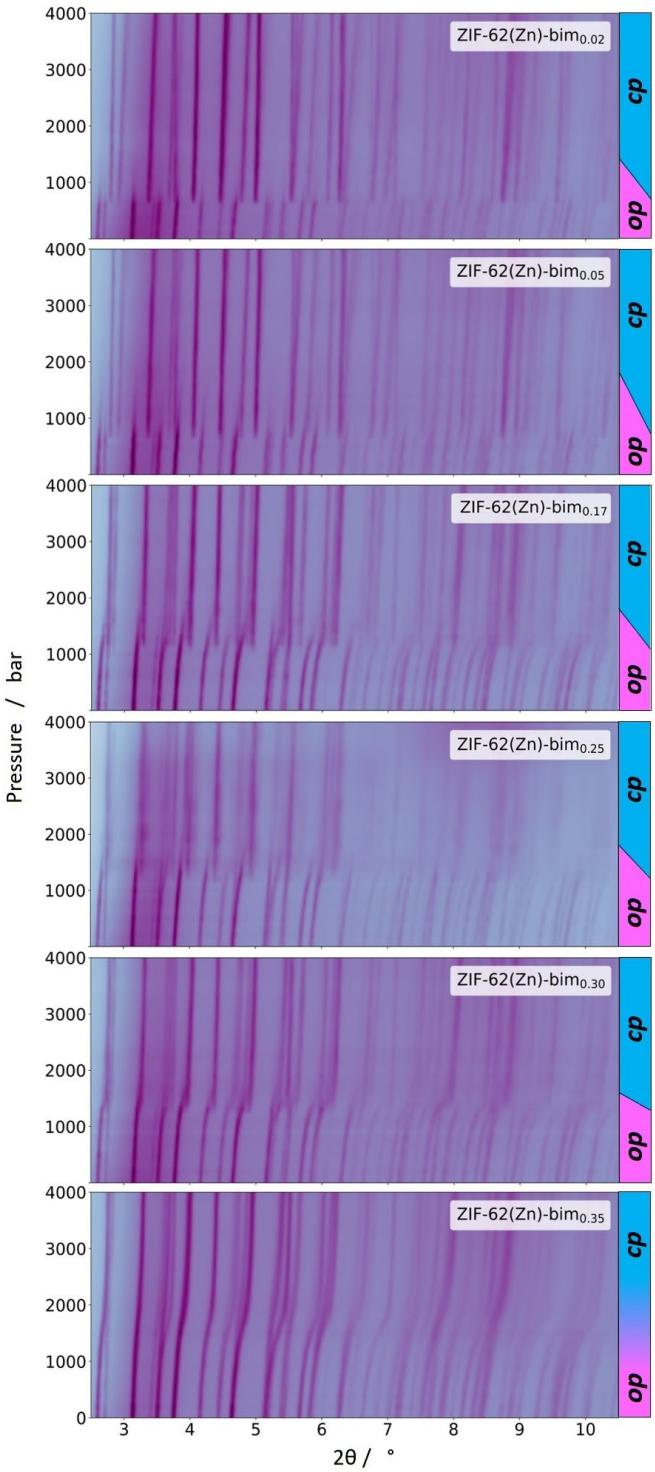

Figure 2. Contour maps of the HP-PXRD patterns of the ZIF-62(Zn)-bim$_x$ samples. Each map is generated from 29 PXRD patterns recorded at pressure points between 1 and 4000 bar. The ***op***-to-***cp*** transition is discontinuous (first order) for $x \leq 0.30$, while it is continuous (second order) for $x = 0.35$. Regions of ***op*** (pink) and ***cp*** (cyan) phase stability and the transition regions are highlighted on the right-hand side.

In order to get a detailed picture of the high-pressure behaviour of this set of solid solutions, the HP-PXRD patterns of each material were sequentially analysed via profile fitting (Le Bail method)[48] starting with the reference parameters from the ***op*** phase derived from single-crystal X-ray diffraction. The ***cp*** phases have been fitted starting with unit cell parameters derived from the published low-temperature ***cp*** phase of ZIF-4.[33] The derived evolution of the unit cell volumes with pressure, the total volume change upon compression from ambient to 4000 bar, as well as the phase-transition regions are displayed in Figure 3. We observed the following trends for the HP behaviour of the ZIF-62(Zn)-bim$_x$ materials as a function of x:

(i) The threshold pressure for the ***op***-to-***cp*** transition increased continuously with increasing x from 700 bar for $x = 0.02$ to 1300 bar for $x = 0.30$. Note, the threshold pressure for the transition of ZIF-4(Zn) (i.e., $x = 0$) was determined to 500 bar in a previous study using the same experimental setup and PTM.[39]

(ii) The transition region where both phases ***op*** and ***cp*** are present initially gets broader from $x = 0.02$ to $x = 0.05$, then gets much narrower again with a further increase of x and finally completely disappears for $x = 0.35$.

(iii) While the unit cell volume of the ***op*** phase at 1 bar is similar for the entire series of materials (4287.1(3) Å^3 to 4341.7(4) Å^3), the unit cell volume of the ***cp*** phase at 4000 bar increases from 3248.4(8) Å^3 for $x = 0.02$ to 3635.5(10) Å^3 for $x = 0.35$. The overall compression at

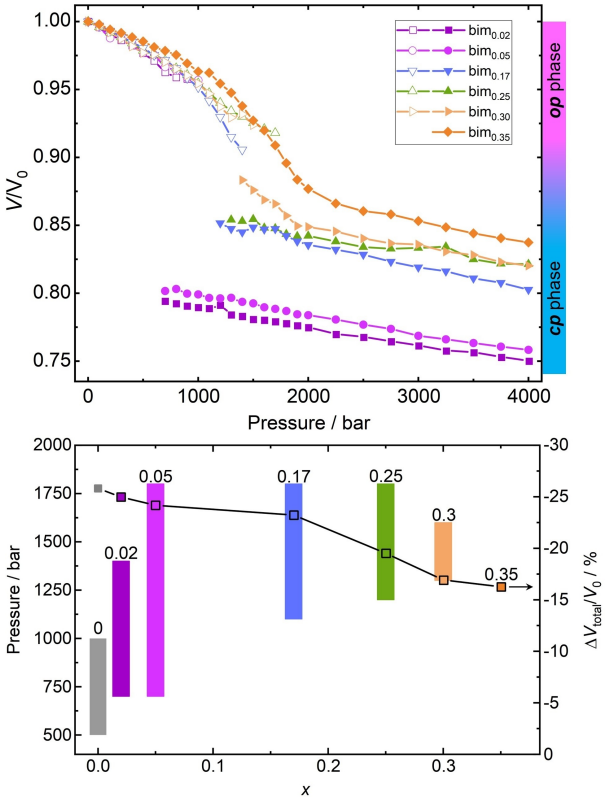

Figure 3. Top: relative volume of the ZIF-62(Zn)-bim$_x$ materials as a function of mechanical pressure. Bottom: transition pressure range (bars) and overall volume contraction (i.e., relative volume change from 1 to 4000 bar, square symbols) of ZIF-62(Zn)-bim$_x$. Literature data of the prototypical ZIF-4 (i.e., $x = 0$) are included for comparison.[39] Lines are visual guides.

4000 bar is 24.8% for $x=0.02$ and 16.7% for $x=0.35$. Likewise, the volume change ΔV across the phase transition gets smaller with increasing x.

These findings corroborate that the exchange of already small amounts of im^- against bim^- in the ZIF-4/ZIF-62 system results in a significant reinforcement of the framework and thus a shift of the transition pressure. Naturally, the ***cp*** phases of the materials that exhibit a higher bim^- content possess a larger unit cell volume because the bulkier bim^- linkers require more space, thus preventing further contraction of the frameworks. The larger pressure range of the ***op***-to-***cp*** transition region of the materials with $x=0.02$ and $x=0.05$ might originate from an increased heterogeneity of these samples on a local scale (i.e., nanoscale regions of higher or lower bim^- content than the average x). Narrowing of the transition range with a further increase in x suggests a more homogeneous distribution of the bim^- linkers throughout the crystals.

As is typical for transitions of flexible MOFs, the ***op***-to-***cp*** transition is first order (i.e., it exhibits a discontinuous volume change) for all compounds with $x\leq 0.30$. This is evident by the disappearance of the reflections belonging to the ***op*** phase in parallel to the appearance of the reflections belonging to the ***cp*** phase in the regions of the phase transition. Remarkably, the situation is very different for $x=0.35$. The reflections associated with the ***op*** phase smoothly shift to higher Bragg angles and continuously transform to the diffraction pattern of the ***cp*** phase. This behaviour is denoted as a second-order phase transition and involves a continuous change in volume. While the materials with $x\leq 0.30$ exhibit both ***op*** and ***cp*** phases in varying quantities during the first-order ***op***-to-***cp*** phase transition, the material with $x=0.35$ only possess a well-defined single phase at each pressure. In a thermodynamic picture, the substitution of more and more im^- by bim^- in the ZIF-62 framework makes the potential energy surface of the system flatter, so that more and more states between the ***op*** and the ***cp*** states are available. For $x=0.35$ the material exhibits a continuous range of states between fully open and closed, and each of them is accessible by adjusting the pressure.

Remarkably, the two cobalt-based materials ZIF-62(Co)-$bim_{0.27}$ and ZIF-62(Co)-$bim_{0.37}$ show a phase behaviour analogous to the corresponding ZIF-62(Zn)-bim_x materials exhibiting a similar x, however, with increased transition pressures. ZIF-62(Co)-$bim_{0.27}$ undergoes a discontinuous first-order ***op***-to-***cp*** phase transition starting at 1700 bar, which is about 500 bar higher than the ZIF-62(Zn)-$bim_{0.25}$. The derivative ZIF-62(Co)-$bim_{0.37}$ again shows a continuous second-order ***op***-to-***cp*** transition comparable to ZIF-62(Zn)-$bim_{0.35}$. The higher phase-transition pressure of the cobalt-based ZIFs may be explained by slightly stronger and more directional ligand-to-metal bonding for ZIF-62(Co)-bim_x compared to ZIF-62(Zn)-bim_x. This is reasoned because of the higher electronegativity (1.65 for Zn and 1.88 for Co) and different valence electron configuration ($3d^{10}$ for Zn^{2+} vs $3d^7$ for Co^{2+}) of cobalt.[19]

It is worth mentioning that all the pressure-induced ***op***-to-***cp*** phase transitions of the studied ZIF-62(M)-bim_x materials are fully reversible after pressure release to ambient pressure. Moreover, we conducted cyclic pressure jump experiments for selected representatives by repetitive cycling between 1 bar and 4000 bar (Figure 4; Section S9). The data demonstrate that the materials repeatedly undergo the ***op***-to-***cp*** phase transition without any loss of crystallinity. Furthermore, the peak width of the reflections does not change significantly during pressure cycling, suggesting that reduction of crystallite size and formation of microstrain are absent (Figure S40).

Bulk Moduli and Compressibility

Based on empirical fits to the pressure-dependent unit cell parameters derived from the profile fits of the HP-PXRD patterns, we determined the pressure-dependent linear compressibilities, volume compressibilities and bulk moduli, as well as the compression work for all ZIF-62(M)-bim_x materials (Sections S11 and S12). The pressure–volume work done on the frameworks upon increasing the pressure from ambient to 4000 bar lies between 18 and 25 $J\,g^{-1}$ (Figure S98). The energy stored in the frameworks in the pressure range up to 4000 bar is generally lower for higher values of x. This indicates that the shift of the phase transition to higher pressures is counterbalanced by the lower volume change ($\Delta V_{total}/V_0$) with increasing x.

The bulk moduli (K_0) of the ***op*** phases determined at 1 bar increases from 2.3 ± 0.1 GPa to 4.1 ± 0.5 GPa when x is increased from 0.02 to 0.35. This finding confirms the increased stiffness of the frameworks with advancing exchange of im^- against bim^-. Upon increasing pressure, the bulk moduli of the ***op*** phases decrease continuously, indicating that the frameworks become more compressible when moving towards the ***op***-to-***cp*** phase transformation (Figure S97). Even though such a pressure-softening behaviour is unusual for conventional solids, it has been observed for other porous framework compounds[49,51] and can further be regarded as a sign for pressure-induced flexibility (i.e., a phase transition). Naturally, the bulk moduli of the corresponding ***cp*** phases at elevated pressure (4000 bar) are larger (4.00 ± 0.45 GPa to 8.81 ± 1.49 GPa), reflecting their denser, non-porous framework structures.

We discuss the unusual compressibility of the continuously contracting ZIF-62(Zn)-$bim_{0.35}$ in more detail here. The V vs p curve of ZIF-62(Zn)-$bim_{0.35}$ (Figure 3) shows that the material compresses by only about 3.8% in the lower pressure range from 0 to 1100 bar (the lowest compression of all materials reported herein). In the intermediate range from 1200 to 2000 bar the framework possesses a remarkably strong response to pressure, involving a contraction by a further 8.6%. Above 2000 bar the framework is in the ***cp*** phase and contracts by another 3.9% until a pressure of 4000 bar is reached. In the intermediate range from 1200 to 2000 bar, where ZIF-62(Zn)-$bim_{0.35}$ shows its strongest response to mechanical pressure, the volumetric compressibility increases from about 800 TPa^{-1} to over 1300 TPa^{-1}, which is equivalent to bulk moduli between only 1.2 and 0.75 GPa. These extremely low bulk

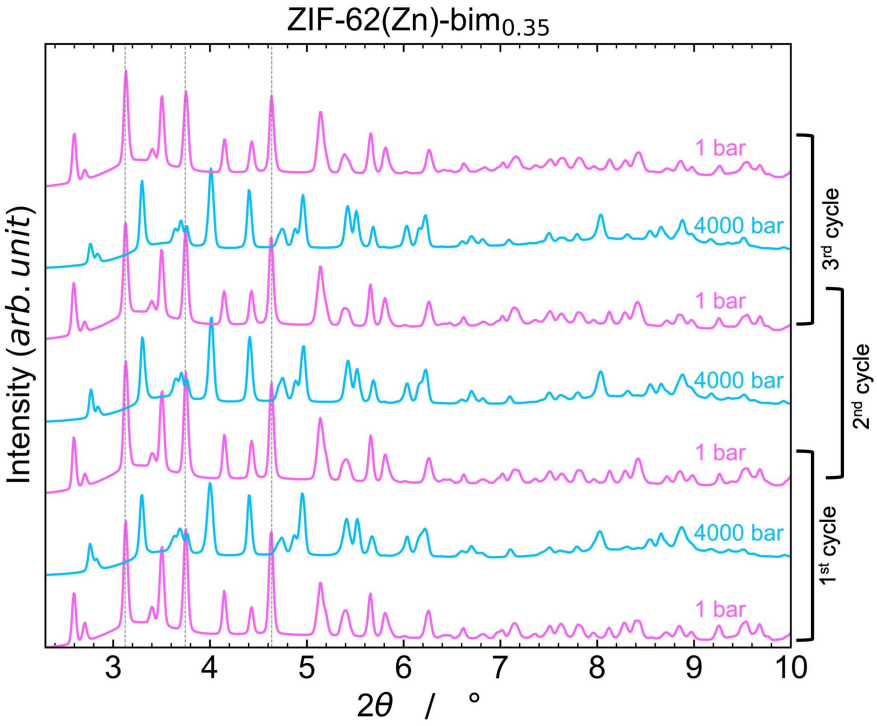

Figure 4. Stacked HP-PXRD patterns recorded via cyclic pressure jumping of ZIF-62(Zn)-bim$_{0.35}$ between 1 bar (pink, ***op*** phase) and 4000 bar (cyan, ***cp*** phase).

moduli are lower than the bulk moduli of other highly flexible MOFs (e.g. 2.0–7.7 GPa for ZIF-4(Zn) and 2.0 GPa for MIL-53(Cr))[24,26] and more comparable to the bulk moduli of liquids (at 20 °C and 1 bar the bulk modulus of methanol is about 0.82 GPa[52]), which corroborates the ultrahigh compressibility of this flexible framework in the continuous phase-transition region.

Structural Refinement and Analysis

In contrast to high-pressure single-crystal X-ray diffraction analysis, atomistic refinements of MOF structures based on HP-PXRD data are rarely reported, as the data quality obtained by conventional diamond anvil cell experiments is often not of sufficient quality. Given the high data quality of the HP-PXRD patterns recorded with the hydraulic pressure cell, we were able to perform sequential structural refinements (Rietveld method) for the whole pressure range of the HP-PXRD data. We selected the two samples on either end of the spectrum, namely ZIF-62(Zn)-bim$_{0.02}$ (showing the typical first-order ***op***-to-***cp*** transition) and ZIF-62(Zn)-bim$_{0.35}$ (showing the unusual second-order ***op***-to-***cp*** transition). Given the very small amount of bim$^-$ in ZIF-62(Zn)-bim$_{0.02}$, its structure was refined using the reported ***op*** and ***cp*** models of ZIF-4 (i.e., neglecting bim$^-$ in the structural model).[33] The ***op*** phase model was applied in the range from ambient to 600 bar, while the ***cp*** phase model was applied in the range from 700 to 4000 bar. For ZIF-62(Zn)-bim$_{0.35}$ we adopted a simplified structural model with reduced disorder, to keep the refinement tractable (Section S13). Generally, the Rietveld refinements produced very good fits to both sets of experimental data with lattice parameters and unit cell volumes in agreement with the results from the previous structureless profile fits (Table S17, Figures S100 and S101).

Figure 5 shows a simplified graphical representation of the refined crystal structures of ZIF-62(Zn)-bim$_{0.02}$ and ZIF-62(Zn)-bim$_{0.35}$ at 1 bar as well as 4000 bar (see Table 1 for the crystallographic data). The simplified representation displays an unrestricted view on the central 8-ring located on the (100) plane (notice that this is an 8-cycle in the language of network topology).[53] This 8-membered ring is the main characteristic for the open cage in the **cag**

Table 1: Crystallographic data from the Rietveld refinements of the ***op*** and ***cp*** phases of ZIF-62(Zn)-bim$_{0.02}$ and ZIF-62(Zn)-bim$_{0.35}$.

	ZIF-62(Zn)-bim$_{0.02}$		ZIF-62(Zn)-bim$_{0.35}$	
Phase	***op***	***cp***	***op***	***cp***
Pressure	1 bar	4000 bar	1 bar	4000 bar
Space group	*Pbca*	*Pbca*	*Pbca*	*Pbca*
a [Å]	15.4786(15)	14.4068(18)	15.482(4)	14.416(4)
b [Å]	15.4833(11)	14.1610(15)	15.572(3)	14.575(3)
c [Å]	18.0544(13)	15.954(2)	17.967(4)	17.164(5)
V [Å^3]	4326.9(6)	3254.9(7)	4331.8(5)	3606.4(4)
$d_{Zn1\cdots Zn2}$ [Å][a]	5.91(4)	5.75(10)	5.9(2)	5.78(13)
R_{wp}	2.02	4.52	7.17	7.73
R_{Bragg}	1.36	2.48	5.08	5.92
χ^2	0.52	1.14	1.76	1.95

[a] Mean Zn···Zn distance of all four crystallographically independent Zn···Zn distances given with the standard deviation of the mean.

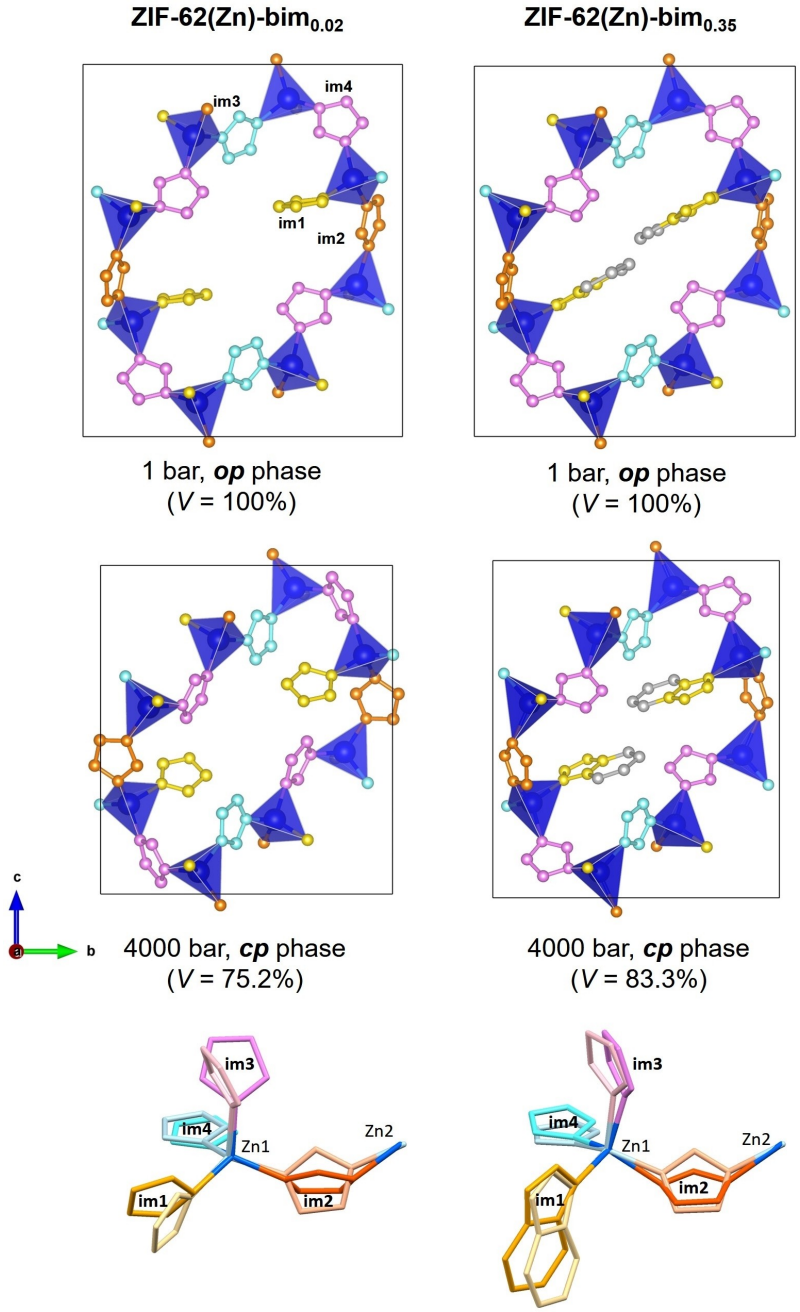

Figure 5. Top: simplified structures of selected ZIF-62(Zn)-bim$_x$ derivatives displaying only the representative 8-membered rings at ambient pressure (***op*** phase) and under 4000 bar (***cp*** phase). All structures are drawn to the same scale. Bottom: an overlay of the asymmetric units of the structures at 1 bar (pale colour) and 4000 bar (vivid colours). The Zn1 and Zn2 atoms of both asymmetric units have been superimposed to visualize the relative changes of the other framework building units.

topology. In analogy to what has been reported for the ***op***-to-***cp*** phase transition of ZIF-4(Zn), the contraction of the ZIF-62(Zn)-bim$_x$ frameworks also involves collective rotations of the im$^-$ and bim$^-$ linkers about the Zn–N coordination bonds, while the Zn···Zn distances contract only slightly (Figure 5, Table 1). For ZIF-62(Zn)-bim$_{0.02}$ the linker rotations happen abruptly during the first-order ***op***-to-***cp*** phase transition at 700 bar. In contrast, ZIF-62(Zn)-bim$_{0.35}$ experiences a continuous rotation of the linkers with increasing mechanical pressure, due to the continuous contraction and the second-order nature of the ***op***-to-***cp*** phase transition (see animations in the Supporting Information). When comparing the ***cp*** phases of both derivatives at 4000 bar, the rotations of the linkers are much less drastic for ZIF-62(Zn)-bim$_{0.35}$ than for ZIF-62(Zn)-bim$_{0.02}$ (Table S18), which is rationalized by the larger steric bulk of the bim$^-$ linker, preventing larger rotations of all the linkers. This is also visualized in the overall contraction of the

frameworks at 4000 bar. ZIF-62(Zn)-bim$_{0.02}$ exhibits only 75.2% of the original volume, while ZIF-62(Zn)-bim$_{0.35}$ possess 83.3% at that pressure. Remarkably, the bim$^-$ linker also influences the direction of rotation for some linkers. Linker **im2**, for example, rotates in opposite directions in ZIF-62(Zn)-bim$_{0.02}$ and ZIF-62(Zn)-bim$_{0.35}$.

Based on the refined crystal structures, we analysed the evolution of the pore volume and the pore size distribution (PSD) of ZIF-62(Zn)-bim$_{0.02}$ and ZIF-62(Zn)-bim$_{0.35}$ as a function of the mechanical pressure with the help of the Zeo++ software package.[54] To get physically meaningful results, the twofold disorder of the bim$^-$ linker enforced by the space group symmetry *Pbca* in the structural model for ZIF-62(Zn)-bim$_{0.35}$ was resolved by converting the Rietveld-refined structures to the subgroup $Pbc2_1$ (Supporting Information). As expected, the pore volume vs pressure curves (Figure 6) show a behaviour very similar to the unit cell volume vs pressure curves (Figure 3 top). ZIF-62(Zn)-bim$_{0.02}$ experiences a slight reduction in pore volume from 0.21 $cm^3 g^{-1}$ to 0.18 $cm^3 g^{-1}$ in the pressure range from ambient to 600 bar (***op*** phase). Upon transition to the ***cp*** phase at 700 bar, the pore volume of the framework immediately reached 0 $cm^3 g^{-1}$. In contrast, ZIF-62(Zn)-bim$_{0.35}$ displayed a continuous reduction of the pore volume

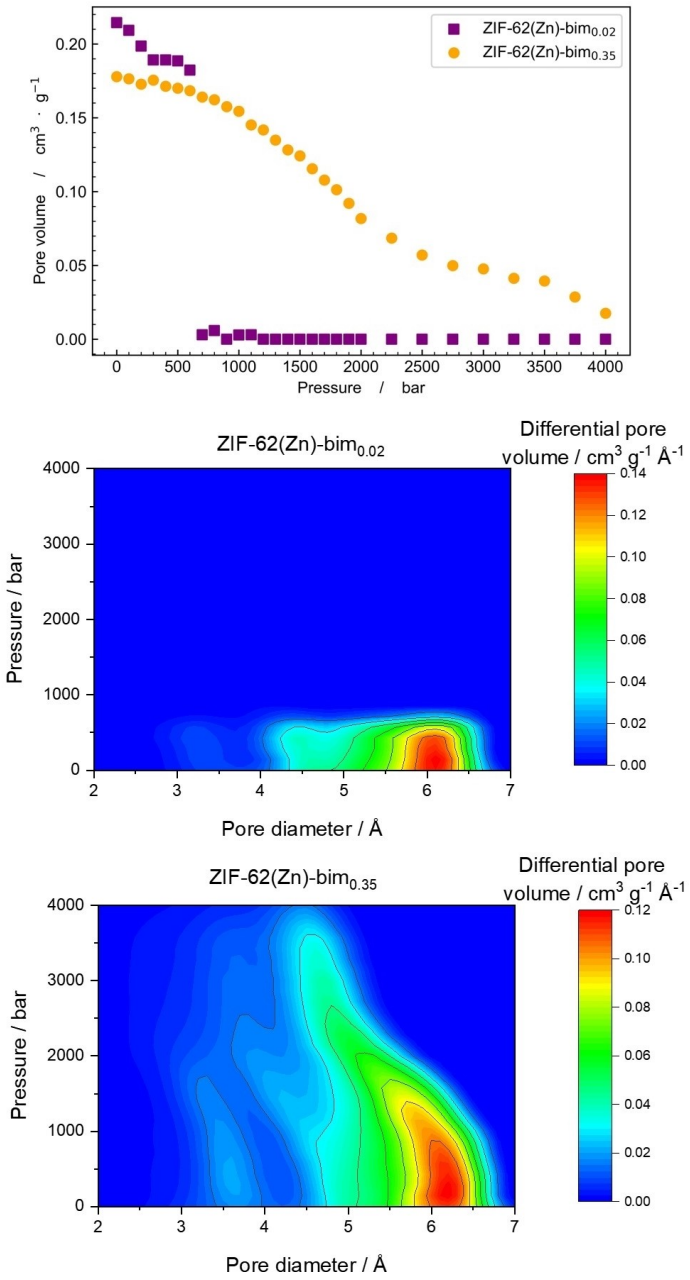

Figure 6. Plot of the pore volume as a function of pressure calculated from the (idealized) crystal structures using Zeo++[54] (top). Visualization of the changes in the PSD with increasing mechanical pressure (bottom). Each contour map was generated from 29 individual PSDs spread over the pressure range from 1 to 4000 bar.

over the entire pressure range from 0.18 $cm^3 g^{-1}$ at 1 bar to 0.02 $cm^3 g^{-1}$ at 4000 bar.

The PSDs calculated from the crystal structures at the various pressures are displayed as contour maps in Figure 6. At ambient pressure, ZIF-62(Zn)-$bim_{0.02}$ and ZIF-62(Zn)-$bim_{0.35}$ have very similar PSDs, ranging from 4 Å to almost 7 Å in pore diameter with a peak at about 6.2 Å. Up to a pressure of 600 bar, the PSDs of both materials showed only minor changes. From 700 bar on, the PSD of ZIF-62(Zn)-$bim_{0.02}$ was featureless because the first-order transition to the ***cp*** phase is associated with the disappearance of porosity. ZIF-62(Zn)-$bim_{0.35}$, however, showed a gradual narrowing of the PSD together with a progressive shift of the maximum pore diameter cut-off from 6.7 Å at 700 bar to only about 5 Å at 3000 bar. This analysis demonstrates that the pore size and the pore-limiting diameter of ZIF-62(Zn)-$bim_{0.35}$ can be precisely adjusted by the application of mechanical pressure, suggesting new possibilities for reversible pore-space modulation of flexible MOFs by a mechanical force. We speculate that the mechanical phase behaviour of ZIF-62(Zn)-$bim_{0.35}$ provides an unusual way to finetune the material's gas sorption selectivity by a mechanical pressure stimulus.[55,56] Given the ease at which gas separation membranes can be prepared from ZIF compounds,[43,57,58] we anticipate that our study sets the stage for the development of ZIF-62 membranes whose separation efficiency is tuneable by mechanical pressure.

Conclusion

We investigated the high-pressure structural behaviour of eight flexible ZIF-62(M)-bim_x derivatives with varying bim^- fractions (x) using powder X-ray diffraction in the range from ambient pressure to 4000 bar. All materials are very soft and feature relatively low bulk moduli between 2.3 and 4.1 GPa at ambient pressure. With increasing mechanical pressure, the ZIF-62(M)-bim_x derivatives undergo a transition from an ***op*** to a ***cp*** phase. The phase transition is reversible for all compounds and can be repeated several times without loss of crystallinity. Most importantly, the transition is discontinuous with respect to the materials' volume (first order) for $x \leq 0.30$, while it becomes continuous (second order) for $0.35 \leq x$. Rietveld refinement on two selected representatives with $x = 0.02$ and $x = 0.35$, provided deep insight into the mechanistic differences of the first- and second-order variants of the ***op***-to-***cp*** phase transition. These insights reveal that the second-order ***op***-to-***cp*** transition allows for the targeted adjustment of the porosity features of the material (pore volume and size) by a specific pressure stimulus, and thus opens the door for the development of gas separation membranes with separation properties (e.g., selectivity, permeance) that can be regulated by mechanical pressure.

The reversibility and repeatability of the ***op***-to-***cp*** phase transition of the ZIF-62 materials is particularly encouraging for their application as nanodampers and shock absorbers. In the form of nanoparticles, these materials may further be useful as functional additives in tribological applications. Furthermore, we anticipate that selectively tuning the mechanical phase behaviour of flexible MOFs, as demonstrated herein by simply mixing linkers with different steric demands, offers an effective approach for optimizing the enthalpy and entropy change across pressure-driven ***op***-to-***cp*** phase transitions. Synthetic maximization of the entropy change of such phase transitions could open the door for the application of such flexible MOFs as barocalorics.

Supporting Information: Deposition Numbers 2130178—2130185 (for single-crystal data), 2130193—2130221 (for pressure-resolved crystal structures of ZIF-62(Zn)-$bim_{0.02}$) and 2130225—2130253 (for pressure-resolved crystal structures of ZIF-62(Zn)-$bim_{0.35}$) contain the supplementary crystallographic data for this paper. These data are provided free of charge by the joint Cambridge Crystallographic Data Centre and Fachinformationszentrum Karlsruhe Access Structures service. Details on synthetic procedures, analytical methods, IR and ^1H NMR spectroscopy data, VT-PXRD and further HP-PXRD data can be found in the Supporting Information. Idealized pressure-resolved crystal structures of ZIF-62(Zn)-$bim_{0.35}$ with resolved disorder are provided in CIF format. Animations of the phase behaviour of ZIF-62(Zn)-$bim_{0.02}$ and ZIF-62(Zn)-$bim_{0.35}$ are available in GIF format.

Acknowledgements

This project received funding from TU Dortmund, Deutsche Forschungsgemeinschaft (447344931 and Priority Programme SPP1928 COORNETs) and the Max Buchner Research Foundation (Grant Number 3699). J.S. acknowledges the China Scholarship Council and P.K. acknowledges the Fonds der Chemischen Industrie for doctoral fellowships. C.L.H. thanks the University of Edinburgh for a Chancellor's Fellowship. The research leading to these results has been supported by the project CALIPSOplus under the Grant Agreement 730872 from the EU Framework Programme for Research and Innovation HORIZON 2020. We thank Diamond Light Source (DLS) for access to beamline I15 (experiment number CY21603-3). Beamline scientist Dr. Annette Kleppe is acknowledged for support with the HP-PXRD experiments at DLS. We acknowledge DESY (Hamburg, Germany), a member of the Helmholtz Association HGF, for the provision of experimental facilities. Parts of this research were carried out at PETRA III on beamline P02.1 (proposal I-20170615) and we thank Dr. Michael Wharmby for assistance. Marvin Kloß is acknowledged for helping with the VT-PXRD experiments. Open Access funding enabled and organized by Projekt DEAL.

Conflict of Interest

The authors declare no conflict of interest.

Data Availability Statement

The data that support the findings of this study are available in the Supporting Information of this article.

Keywords: High-Pressure Crystallography · Mechanical Properties · Metal–Organic Frameworks · Phase Transition · Responsive Materials

[1] A. Darabi, P. G. Jessop, M. F. Cunningham, *Chem. Soc. Rev.* **2016**, *45*, 4391.
[2] R. J. Wojtecki, M. A. Meador, S. J. Rowan, *Nat. Mater.* **2011**, *10*, 14.
[3] J. M. McCracken, B. R. Donovan, T. J. White, *Adv. Mater.* **2020**, *32*, 1906564.
[4] A. Schneemann, V. Bon, I. Schwedler, I. Senkovska, S. Kaskel, R. A. Fischer, *Chem. Soc. Rev.* **2014**, *43*, 6062.
[5] Z. Chang, D.-H. Yang, J. Xu, T.-L. Hu, X.-H. Bu, *Adv. Mater.* **2015**, *27*, 5432.
[6] J. A. Mason, J. Oktawiec, M. K. Taylor, M. R. Hudson, J. Rodriguez, J. E. Bachman, M. I. Gonzalez, A. Cervellino, A. Guagliardi, C. M. Brown, P. L. Llewellyn, N. Masciocchi, J. R. Long, *Nature* **2015**, *527*, 357.
[7] C. M. McGuirk, T. Runčevski, J. Oktawiec, A. Turkiewicz, M. K. Taylor, J. R. Long, *J. Am. Chem. Soc.* **2018**, *140*, 15924.
[8] J. Rodriguez, I. Beurroies, T. Loiseau, R. Denoyel, P. L. Llewellyn, *Angew. Chem. Int. Ed.* **2015**, *54*, 4626; *Angew. Chem.* **2015**, *127*, 4709.
[9] V. Finsy, L. Ma, L. Alaerts, D. E. de Vos, G. V. Baron, J. Denayer, *Microporous Mesoporous Mater.* **2009**, *120*, 221.
[10] N. Yanai, T. Uemura, M. Inoue, R. Matsuda, T. Fukushima, M. Tsujimoto, S. Isoda, S. Kitagawa, *J. Am. Chem. Soc.* **2012**, *134*, 4501.
[11] N. Yanai, K. Kitayama, Y. Hijikata, H. Sato, R. Matsuda, Y. Kubota, M. Takata, M. Mizuno, T. Uemura, S. Kitagawa, *Nat. Mater.* **2011**, *10*, 787.
[12] F.-X. Coudert, *Chem. Mater.* **2015**, *27*, 1905.
[13] A. Schneemann, P. Vervoorts, I. Hante, M. Tu, S. Wannapaiboon, C. Sternemann, M. Paulus, D. F. Wieland, S. Henke, R. A. Fischer, *Chem. Mater.* **2018**, *30*, 1667.
[14] S. Horike, S. Shimomura, S. Kitagawa, *Nat. Chem.* **2009**, *1*, 695.
[15] L. Vanduyfhuys, S. M. J. Rogge, J. Wieme, S. Vandenbrande, G. Maurin, M. Waroquier, V. van Speybroeck, *Nat. Commun.* **2018**, *9*, 204.
[16] S. Henke, A. Schneemann, R. A. Fischer, *Adv. Funct. Mater.* **2013**, *23*, 5990.
[17] R. Pallach, J. Keupp, K. Terlinden, L. Frentzel-Beyme, M. Kloß, A. Machalica, J. Kotschy, S. K. Vasa, P. A. Chater, C. Sternemann, M. T. Wharmby, R. Linser, R. Schmid, S. Henke, *Nat. Commun.* **2021**, *12*, 4097.
[18] I. Schwedler, S. Henke, M. T. Wharmby, S. R. Bajpe, A. K. Cheetham, R. A. Fischer, *Dalton Trans.* **2016**, *45*, 4230.
[19] S. Henke, M. T. Wharmby, G. Kieslich, I. Hante, A. Schneemann, Y. Wu, D. Daisenberger, A. K. Cheetham, *Chem. Sci.* **2018**, *9*, 1654.
[20] P. G. Yot, L. Vanduyfhuys, E. Alvarez, J. Rodriguez, J.-P. Itié, P. Fabry, N. Guillou, T. Devic, I. Beurroies, P. L. Llewellyn, V. van Speybroeck, C. Serre, G. Maurin, *Chem. Sci.* **2016**, *7*, 446.
[21] I. Beurroies, M. Boulhout, P. L. Llewellyn, B. Kuchta, G. Férey, C. Serre, R. Denoyel, *Angew. Chem. Int. Ed.* **2010**, *49*, 7526; *Angew. Chem.* **2010**, *122*, 7688.
[22] P. Iacomi, J. S. Lee, L. Vanduyfhuys, K. H. Cho, P. Fertey, J. Wieme, D. Granier, G. Maurin, V. van Speybroeck, J.-S. Chang, P. G. Yot, *Chem. Sci.* **2021**, *12*, 5682.
[23] P. G. Yot, Z. Boudene, J. Macia, D. Granier, L. Vanduyfhuys, T. Verstraelen, V. van Speybroeck, T. Devic, C. Serre, G. Férey, N. Stock, G. Maurin, *Chem. Commun.* **2014**, *50*, 9462.
[24] P. Vervoorts, J. Stebani, A. S. J. Méndez, G. Kieslich, *ACS Mater. Lett.* **2021**, *3*, 1635.
[25] F. Millange, R. I. Walton, *Isr. J. Chem.* **2018**, *58*, 1019.
[26] A. V. Neimark, F.-X. Coudert, C. Triguero, A. Boutin, A. H. Fuchs, I. Beurroies, R. Denoyel, *Langmuir* **2011**, *27*, 4734.
[27] P. Vervoorts, J. Keupp, A. Schneemann, C. L. Hobday, D. Daisenberger, R. A. Fischer, R. Schmid, G. Kieslich, *Angew. Chem. Int. Ed.* **2021**, *60*, 787; *Angew. Chem.* **2021**, *133*, 800.
[28] S. Henke, A. Schneemann, A. Wütscher, R. A. Fischer, *J. Am. Chem. Soc.* **2012**, *134*, 9464.
[29] J. Wieme, S. M. J. Rogge, P. G. Yot, L. Vanduyfhuys, S.-K. Lee, J.-S. Chang, M. Waroquier, G. Maurin, V. van Speybroeck, *J. Mater. Chem. A* **2019**, *7*, 22663.
[30] G. F. Turner, S. C. McKellar, D. R. Allan, A. K. Cheetham, S. Henke, S. A. Moggach, *Chem. Sci.* **2021**, *12*, 13793.
[31] P. G. Yot, K. Yang, V. Guillerm, F. Ragon, V. Dmitriev, P. Parisiades, E. Elkaïm, T. Devic, P. Horcajada, C. Serre, N. Stock, J. P. S. Mowat, P. A. Wright, G. Férey, G. Maurin, *Eur. J. Inorg. Chem.* **2016**, 4424.
[32] P. G. Yot, Q. Ma, J. Haines, Q. Yang, A. Ghoufi, T. Devic, C. Serre, V. Dmitriev, G. Férey, C. Zhong, G. Maurin, *Chem. Sci.* **2012**, *3*, 1100.
[33] M. T. Wharmby, S. Henke, T. D. Bennett, S. R. Bajpe, I. Schwedler, S. P. Thompson, F. Gozzo, P. Simoncic, C. Mellot-Draznieks, H. Tao, Y. Yue, A. K. Cheetham, *Angew. Chem. Int. Ed.* **2015**, *54*, 6447; *Angew. Chem.* **2015**, *127*, 6547.
[34] A. Phan, C. J. Doonan, F. J. Uribe-Romo, C. B. Knobler, M. O'Keeffe, O. M. Yaghi, *Acc. Chem. Res.* **2010**, *43*, 58.
[35] K. S. Park, Z. Ni, A. P. Côté, J. Y. Choi, R. Huang, F. J. Uribe-Romo, H. K. Chae, M. O'Keeffe, O. M. Yaghi, *Proc. Natl. Acad. Sci. USA* **2006**, *103*, 10186.
[36] Y.-Q. Tian, Y.-M. Zhao, Z.-X. Chen, G.-N. Zhang, L.-H. Weng, D.-Y. Zhao, *Chem. Eur. J.* **2007**, *13*, 4146.
[37] Y.-Q. Tian, Z.-X. Chen, L.-H. Weng, H.-B. Guo, S. Gao, D. Y. Zhao, *Inorg. Chem.* **2004**, *43*, 4631.
[38] P. Iacomi, G. Maurin, *ACS Appl. Mater. Interfaces* **2021**, *13*, 50602.
[39] P. Vervoorts, C. L. Hobday, M. G. Ehrenreich, D. Daisenberger, G. Kieslich, *Z. Anorg. Allg. Chem.* **2019**, *645*, 970.
[40] R. N. Widmer, G. I. Lampronti, S. Chibani, C. W. Wilson, S. Anzellini, S. Farsang, A. K. Kleppe, N. P. M. Casati, S. G. MacLeod, S. A. T. Redfern, F.-X. Coudert, T. D. Bennett, *J. Am. Chem. Soc.* **2019**, *141*, 9330.
[41] R. Banerjee, A. Phan, B. Wang, C. Knobler, H. Furukawa, M. O'Keeffe, O. M. Yaghi, *Science* **2008**, *319*, 939.
[42] L. Frentzel-Beyme, M. Kloß, R. Pallach, S. Salamon, H. Moldenhauer, J. Landers, H. Wende, J. Debus, S. Henke, *J. Mater. Chem. A* **2019**, *7*, 985.
[43] L. Frentzel-Beyme, M. Kloß, P. Kolodzeiski, R. Pallach, S. Henke, *J. Am. Chem. Soc.* **2019**, *141*, 12362.
[44] T. D. Bennett, Y. Yue, P. Li, A. Qiao, H. Tao, N. G. Greaves, T. Richards, G. I. Lampronti, S. A. T. Redfern, F. Blanc, O. K. Farha, J. T. Hupp, A. K. Cheetham, D. A. Keen, *J. Am. Chem. Soc.* **2016**, *138*, 3484.
[45] H. Tao, T. D. Bennett, Y. Yue, *Adv. Mater.* **2017**, *29*, 1601705.
[46] R. A. Young, *The Rietveld method*, Oxford University Press, Oxford, **1993**.
[47] P. Thompson, D. E. Cox, J. B. Hastings, *J. Appl. Crystallogr.* **1987**, *20*, 79.
[48] A. Le Bail, *Powder Diffr.* **2005**, *20*, 316.
[49] S. Dissegna, P. Vervoorts, C. L. Hobday, T. Düren, D. Daisenberger, A. J. Smith, R. A. Fischer, G. Kieslich, *J. Am. Chem. Soc.* **2018**, *140*, 11581.

[50] N. J. Brooks, B. L. L. E. Gauthe, N. J. Terrill, S. E. Rogers, R. H. Templer, O. Ces, J. M. Seddon, *Rev. Sci. Instrum.* **2010**, *81*, 064103.
[51] K. W. Chapman, G. J. Halder, P. J. Chupas, *J. Am. Chem. Soc.* **2009**, *131*, 17546.
[52] M. Taravillo, F. J. Pérez, J. Núñez, M. Cáceres, V. G. Baonza, *J. Chem. Eng. Data* **2007**, *52*, 481.
[53] V. A. Blatov, M. O'Keeffe, D. M. Proserpio, *CrystEngComm* **2010**, *12*, 44.
[54] T. F. Willems, C. H. Rycroft, M. Kazi, J. C. Meza, M. Haranczyk, *Microporous Mesoporous Mater.* **2012**, *149*, 134.
[55] N. Chanut, A. Ghoufi, M.-V. Coulet, S. Bourrelly, B. Kuchta, G. Maurin, P. L. Llewellyn, *Nat. Commun.* **2020**, *11*, 1216.
[56] H. Zhao, G. Maurin, A. Ghoufi, *J. Chem. Phys.* **2021**, *154*, 084702.
[57] A. Knebel, B. Geppert, K. Volgmann, D. I. Kolokolov, A. G. Stepanov, J. Twiefel, P. Heitjans, D. Volkmer, J. Caro, *Science* **2017**, *358*, 347.
[58] Y. Wang, H. Jin, Q. Ma, K. Mo, H. Mao, A. Feldhoff, X. Cao, Y. Li, F. Pan, Z. Jiang, *Angew. Chem. Int. Ed.* **2020**, *59*, 4365; *Angew. Chem.* **2020**, *132*, 4395.

Manuscript received: December 23, 2021
Accepted manuscript online: February 4, 2022
Version of record online: March 24, 2022